RESEARCH ARTICLE

High-throughput screening of sulfur-based silver superionic conductors

Zhaobin Zhang, Jianfu Li*, Yang Lv, Yong Liu, Jianan Yuan, Jiani Lin, Xiaoli Wang*

School of Physics and Electronic Information, Yantai University, Yantai 264005, China

Corresponding authors. E-mail: jianfuli@ytu.edu.cn, xlwang@ytu.edu.cn

Received June 12, 2026; accepted August 10, 2026

Supporting Information

Supplementary Note 1

Details of MLFF Calculation

Furthermore, the combination of first principles and molecular dynamics methods enables us to achieve the desired accuracy and predictive capabilities. However, long simulation times and the requirement for large supercell sizes remain obstacles to obtaining ideal results in these calculations. Recently, the use of MLFF has emerged as a favorable solution, allowing for a significant increase in the size of supercells in molecular dynamics simulations while maintaining first-principles accuracy[1–3]. The potential energy in the MLFF is described as a function of material atomic structure descriptors with parameters. This function is optimized to accurately reproduce the total energy, forces, and stress tensor components of the first-principles training data. The developed MLFF can be effectively utilized in molecular dynamics and Monte Carlo simulations, enabling efficient estimation of finite-temperature material properties that are nearly equivalent to those obtained from first-principles calculations. A notable advantage of this method is its significant reduction in required human intervention during the construction process compared to traditional classical potential functions. Simultaneously, the required timescales for simulations can be substantially reduced. The application of this approach, leveraging machine-learned force fields in dynamic simulations, has demonstrated success in various studies[4–16].

On-the-fly training is based on MD simulations to sample training structures. Piece by piece a data set is automatically assembled and used to generate an MLFF whenever feasible. Conversely, at each time step the current force field predicts energy, forces and the corresponding Bayesian error estimations. Simply put, if the error is above a certain threshold another ab-initio calculation is performed and the reference energy and forces are added to the training data set. In the opposite case, the ab-initio step is omitted and the system is propagated via MLFF predictions. As the force field gets better along the trajectory many ab-initio steps can be avoided and the MD simulation is significantly accelerated. Ultimately, the on-the-fly training results in an MLFF which is ready for production, i.e., running an MD simulation in prediction-only mode. The following steps outline the path from start to production run:

Step 1: Prepare molecular dynamics run,

Step 2: Start on-the-fly training from scratch,

Step 3 (optional): Continue on-the-fly training from existing training database,

Step 4: Refit for fast prediction mode,

Step 5: Applying the machine-learned force field in production runs.

The error values of the MLFF in this work are shown in Supplementary Fig.S1. All the errors are within a reasonable range.

Topological analysis

A topological analysis of the structure was conducted using Zeo++ to identify the LCD[17]. The removal of all Ag ions from the crystal structure was followed by the conduction of a topological analysis on the 4x4x4 supercell crystal structure network, which resulted in the identification of three distinct types of pores. The LCD was then selected for topological research, and the pore size was screened based on the radius of the Ag ion (larger than the Ag ion radius). It is imperative to ensure that Ag ions are able to move freely within the crystal structure.

High-throughput screening of Ag-ion compounds

Step 1. Basic Materials Check. Firstly, we obtained the ternary sulfides containing Ag from the Materials Project database[18] by pymatgen software[19]and made a preliminary screening: structures with more than 30 atoms were excluded. After this screening step, a total of 130 sulfides were obtained;

Step 2. Element screening based on resource abundance and Ag-anode electrochemical stability. We eliminate structures containing Co, V, Au, Pb, Hg, Cd, As, Tl, Be, Th, U, Rh, Ir and Pu for the following reasons: Co and V suffer from scarce mineral resources and severe irreversible redox side reactions with Ag metal; the rest possess high toxicity, radioactivity or extreme air sensitivity. Fe and Cr are retained owing to rich crust reserves and stable interfaces with Ag anodes, even with mild magnetic-lattice modulation effects. After this filtering step, 93 sulfide structures were retained for subsequent topological analysis;

Step 3. Perform topological analysis of the 93 sulfides that have been filtered using Zeo++ and conduct LCD analysis on the 4×4×4 supercells after removing Ag atoms. Different coordination numbers of Ag ions will result in different differences in ionic radii. Based on Shannon Radii[20,21], we make reasonable selections and screen the obtained structures for coordination numbers of Ag ions ranging from 2 to 5, with Ag ion radii between 0.67 and 1 Å. Considering that ions need channels larger than their own diameters during diffusion, we further apply the important screening descriptor of LCD ≥ 1.8 Å, in combination with the channel size selections from previous studies on other superionic states[22]. After this step, we obtained 43 sulfides；

Step 4. The initial stage of this process involves the screening of high coordination numbers and the conducting of MLFF simulation of the obtained crystal structures. In order to prevent the high coordination number crystal structures from also having the superionic state, the structures that might have the superionic state were selected from the structures screened in the previous step and MLFF simulation was conducted with the obtained sulfides.

Supplementary Note 2

Why choose LCD as the descriptor?

The existence of ion diffusion channels is imperative for the formation of superionic states, yet the identification of suitable channels remains a formidable challenge. Although overly large ion diffusion channels can significantly weaken the interaction between ions and lower the energy barrier for ion diffusion, the structure of the material can become unstable at high temperatures, leading to crystal collapse. Conversely, the presence of narrow channels has been shown to have the capacity to enhance the Coulomb repulsive force, increase the energy barrier, and impede the migration of ions[23]. In order to identify the suitable materials capable of forming superionic states, the Zeo++ software was utilised for topological analysis. LCD was selected as the characteristic descriptor in order to screen superionic conductors of sulfur-based silver compounds. LCD is the term given to the maximum radius of a sphere that can be accommodated along the free sphere path. This concept is employed to measure the diffusion space size of ions in crystal structures. LCD is indicative of the maximum aperture of the diffusion channel; as such, it is of significant importance in the research of ionic and superionic conductors. The parameters of the largest included sphere and the largest free sphere are shown as in Figure 1. The larger LCD results in wider internal ion migration channels, thereby promoting the diffusion of ions.

In order to verify the hypothesis that the LCD can be used as a feasible descriptor, the known Li and Ag ionic superionic conductors were tested. It was established that the LCD value of these materials is generally greater than 2

Å (see Table.S1). Furthermore, the superionic transition temperature of these materials is generally low, with the majority of materials exhibiting a superionic transition temperature close to or lower than room temperature. In earlier research, the ionic conductivity of these superionic materials was typically found to be greater than 10^{-3} S/cm, thereby demonstrating their excellent ionic conductivity at room temperature[19,24–28]. It can be hypothesized that as the LCD value decreases, the superionic state transition temperature will also increase accordingly. This finding underscores the significance of the large LCD value in the screening of superionic conductor materials.

Table S1 | LCD of $Li^+/Ag^+/Na^+/K^+$ superionic state compounds.

Compound	LCD (Å)	ref
$Li_{10}GeP_2S_{12}$	2.166	[24]
$Ag_4Sn_3S_8$	2.175	[26]
AgI	2.170	[29,30]
Li_4SnS_4	2.105	[31]
Li_4GeS_4	2.049	[31]
Na_3PS_4	2.114	[32]
Na_3SbS_4	2.278	[33]
$NaNbCl_6$	2.165	[34]
$NaTaCl_6$	2.164	[34]
K_2CdO_2	2.369	[35]
K_3SbS_4	2.861	[36]
$K_4P_2O_7$	3.787	[37]

In comparison with conventional screening methodologies, LCD as a feature descriptor not only facilitates the screening process, but also enables more precise prediction of the ionic conductivity and superionic state transition characteristics of materials. Through theoretical calculations, we are able to effectively identify materials with suitable channel sizes, thus overcoming the lengthy and inaccurate problems that may occur in other screening methods to a certain extent. Subsequent testing and comparison of the research results demonstrate that LCD can provide substantial support for the screening of sulfur silver compounds. Moreover, the results of this study furnish a feasible direction for the design of other ionic conductive materials, and the analysis of the explained ion transport path provides a reference point for the study of other superionic phenomena.

Supplementary Note 3

The structures that were selected for further investigation primarily comprise layered structures and complex three-dimensional structures. It has been determined that the LCD descriptor is highly efficient in the screening of materials with superionic states. The findings of this study demonstrate that the transition temperature of the superionic state increases in proportion to the decrease in LCD. It is noteworthy that the selected structures exhibit high ionic conductivity (>10^{-3} S/cm), yet further analysis is required to ascertain their practical applications. Although the energy barrier can directly reflect the difficulty of Ag ion migration, its magnitude is influenced by multiple factors.

For instance, a dense atomic arrangement, a paucity of defects, and strong inter-ion interactions can all result in an increase in the energy barrier. Consequently, the reduction of the energy barrier is identified as a pivotal strategy to enhance the migration rate of ions or molecules and thereby improve material performance. In disciplines such as solid-state electrolytes, catalyst design and materials science, the reduction of energy barriers is of paramount importance in enhancing ionic conductivity, catalytic efficiency and material reactivity. While elevated temperatures can indeed surmount these constraints, they concomitantly impose stringent limitations on the applicability of the materials in question. The introduction of defects has emerged as a prevalent strategy to reduce energy barriers, particularly effective for structures with a paucity of vacancy defects. However, it is important to note that the introduction of defects can compromise the structural stability of materials, especially at high temperatures, potentially leading to material degradation. In our previous research, the introduction of Ag defects was found to have a significant effect on the superionic state transition temperature of $AgAlO_2$ and $AgFeO_2$. Consequently, it is imperative to identify an appropriate range for material modification. Concurrently, the sublattice structure configuration and associated factors have the capacity to exert influence on the superionic state transition temperature. The degree of sublattice distortion, in conjunction with diverse configurations and other variables, has the potential to influence the superionic state transition temperature. Furthermore, it was determined that during the MLFF simulation, the layered structure would fluctuate. It is hypothesised that this fluctuation would cause changes in the channels within the structure, making the distribution of electrons more uniform and thereby reducing the energy barrier, ultimately facilitating the diffusion of Ag ions. For an alternative configuration, the sublattices would also vibrate within a stable range. This behaviour might also lead to a more uniform distribution of electrons within the structure, and the sublattices would undergo varying degrees of distortion, which could potentially provide larger channels for the diffusion of Ag ions. The present study has investigated these potential factors. Furthermore, while ion migration has been explored through MLFF simulations and first-principles calculations, these computational models have not yet incorporated all the complex factors present in real materials, such as surface effects and the macroscopic structure of the material. In practical applications, these factors may also significantly affect the performance of electrical conductivity.

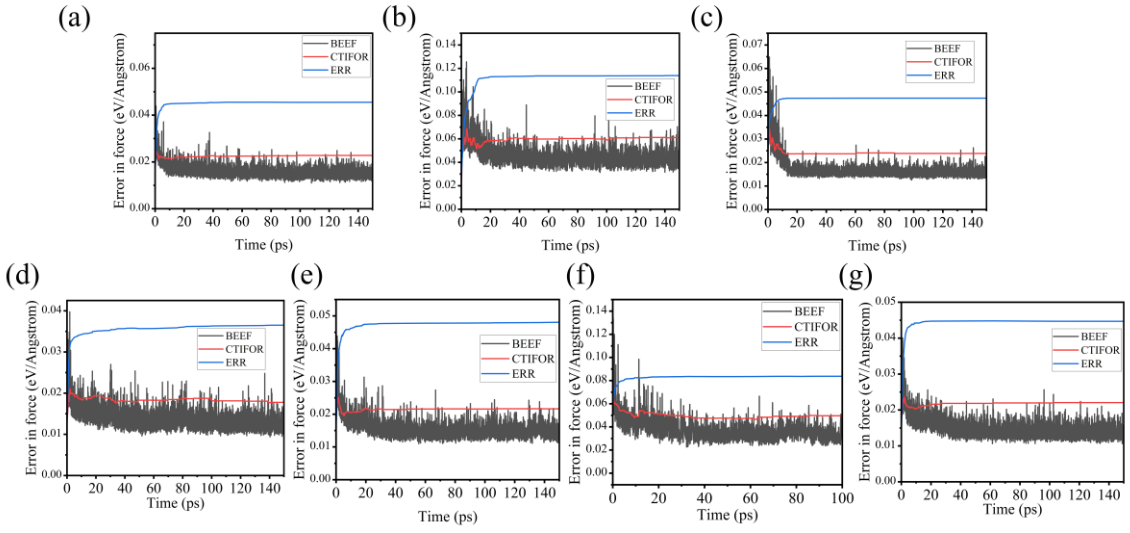

Fig. S1 The error for each structure simulation by MLFF method. All the errors are within the reasonable range. (a) The error of the machine learning force field (MLFF) for Ag_6NbS_6;(b) The error of the machine learning force field (MLFF) for Ag_5SbS_4;(c) The error of the machine learning force field (MLFF) for $AgCrS_2$;(d) The error of the machine learning force field (MLFF) for Ag_9AlS_6;(e) The error of the machine learning force field (MLFF) for Ag_7NbS_6;(f) The error of the machine learning force field (MLFF) for $AgFeS_2$;(g) The error of the machine learning force field (MLFF) for Ag_7TaS_6.

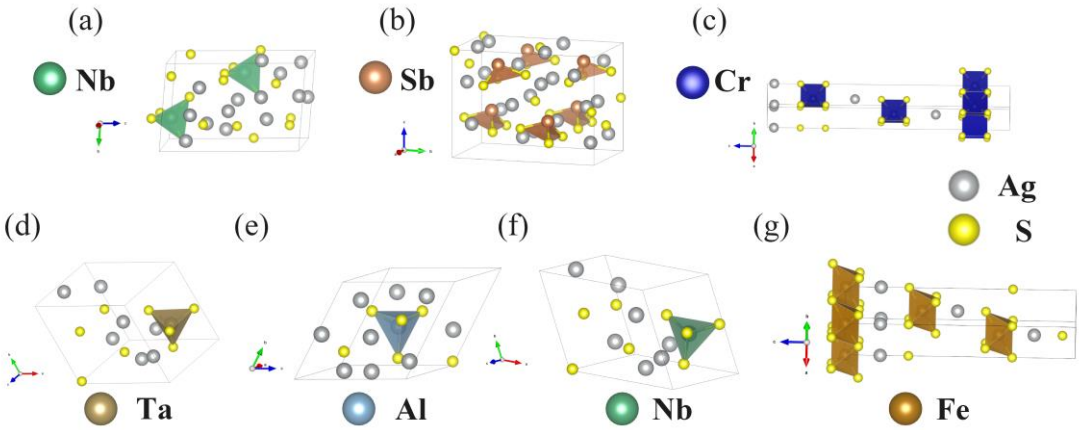

Fig. S2 The structures identified through high-throughput screening. (a) The structure of Ag_6NbS_6; (b) The structure of Ag_5SbS_4 ; (c) The structure of $AgCrS_2$; (d) The structure of Ag_7TaS_6 ; (e) The structure of Ag_9AlS_6; (f) The structure of Ag_7NbS_6; (g) The structure of $AgFeS_2$.

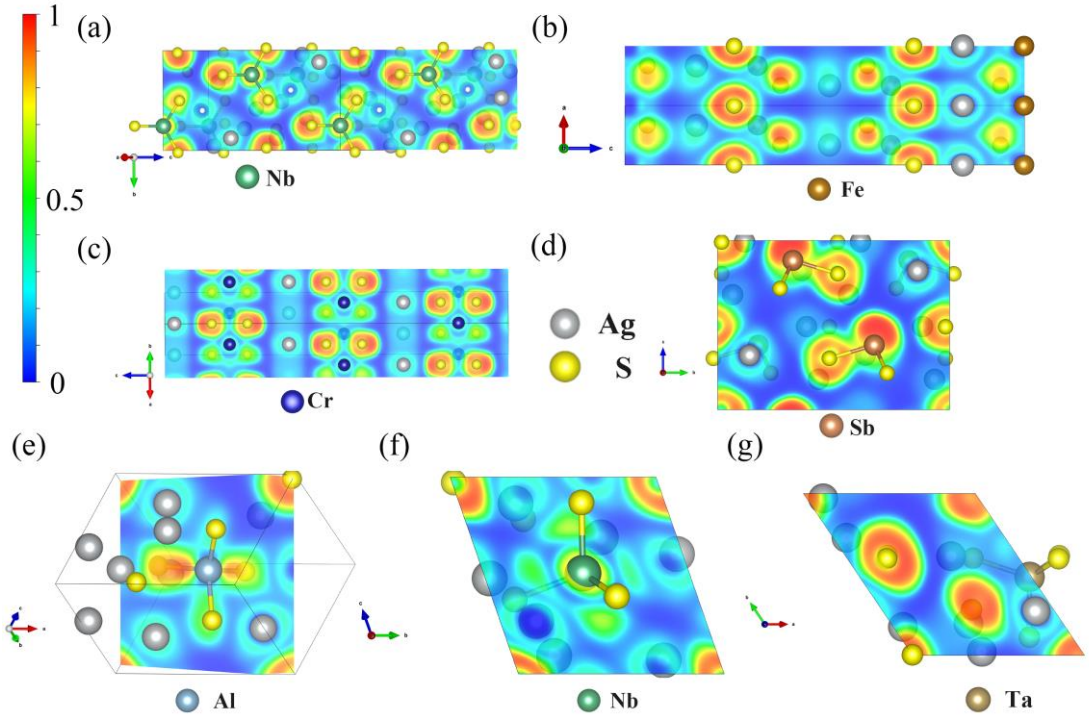

Fig. S3 The electron localization function (ELF) of the structures obtained through high-throughput screening. There is no obvious electron localization between Ag examples and other ions. ELF diagrams of all structures including (a) Ag_6NbS_6, (b) $AgFeS_2$, (c) $AgCrS_2$, (d) Ag_5SbS_4, (e) Ag_9AlS_6, (f) Ag_7NbS_6, and (g) Ag_7TaS_6.

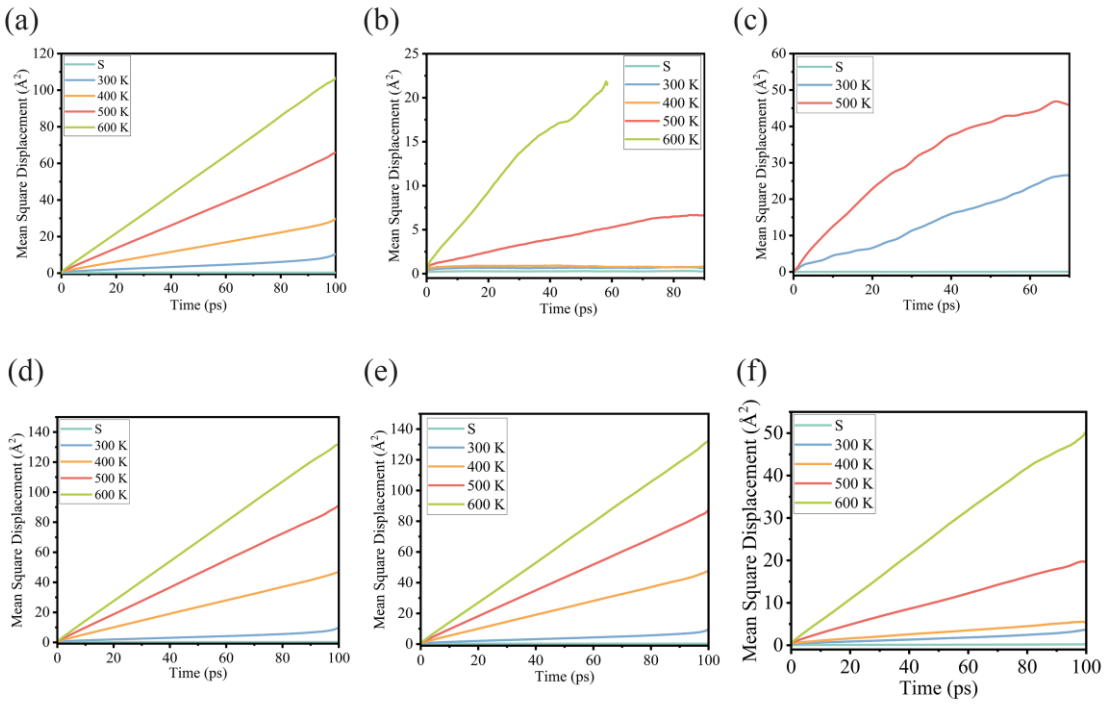

Fig. S4 The mean square displacements (MSD) of these structures: (a) Ag_6NbS_6, (b) Ag_5SbS_4, (c) $AgCrS_2$, (d) Ag_7TaS_6, (e) Ag_7NbS_6, (f)$AgFeS_2$.

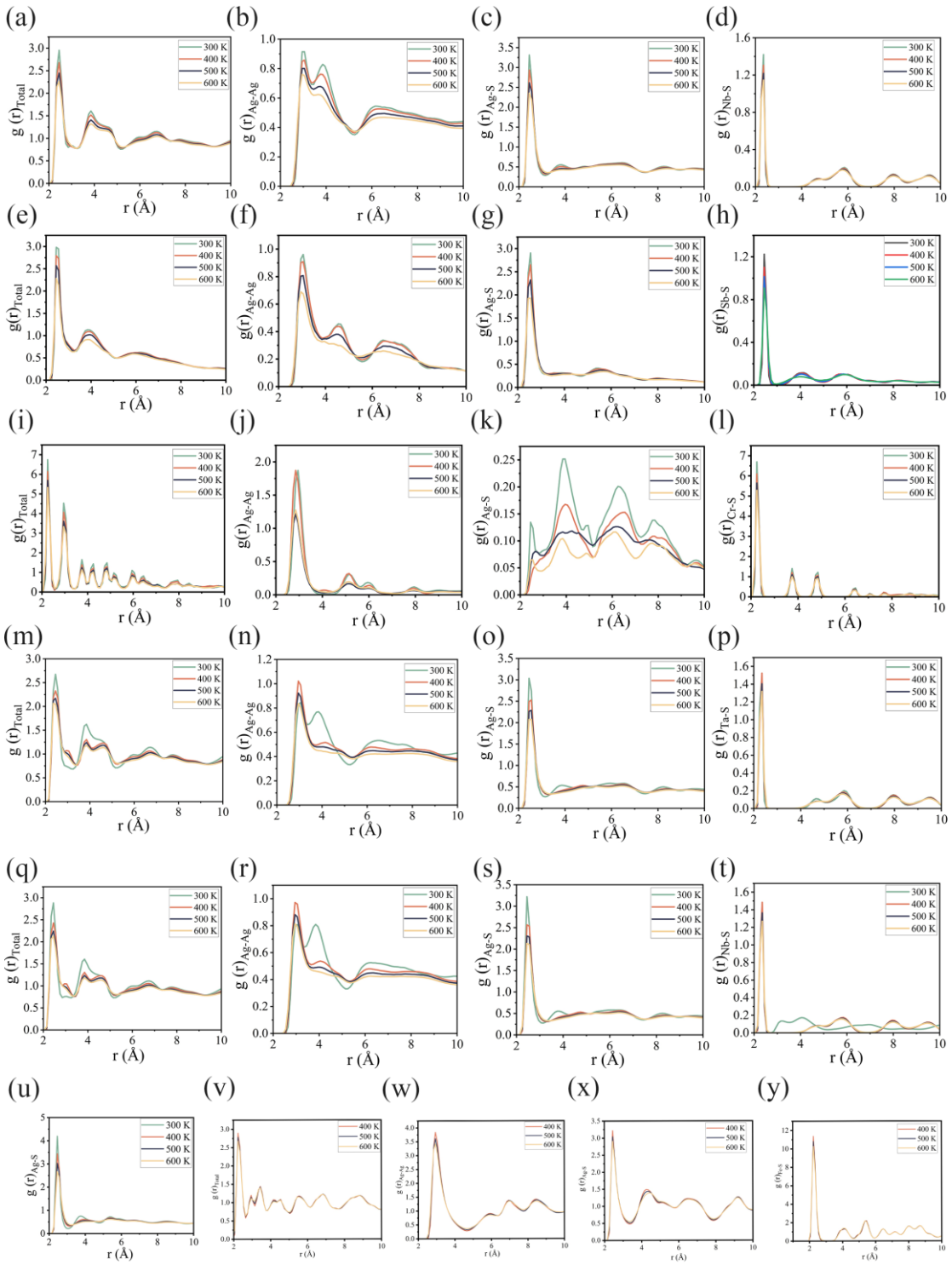

Fig. S5 (a)-(d) Radial distribution functions (RDF) of Ag_6NbS_6 at different temperatures and different distances; (e)-(h) Radial distribution functions (RDF) of Ag_5SbS_4 at different temperatures and different distances; (i)-(l) Radial distribution functions (RDF) of $AgCrS_2$ at different temperatures and different distances; (m)-(p) Radial distribution functions (RDF) of Ag_7TaS_6 at different temperatures and different distances; (q)-(t) Radial distribution functions (RDF) of Ag_7NbS_6 at different temperatures and different distances; (u) Radial distribution functions (RDF) of Ag_9AlS_6 at different temperatures and different distances; (v)-(y) Radial distribution functions (RDF) of $AgFeS_2$ at different temperatures and different distances

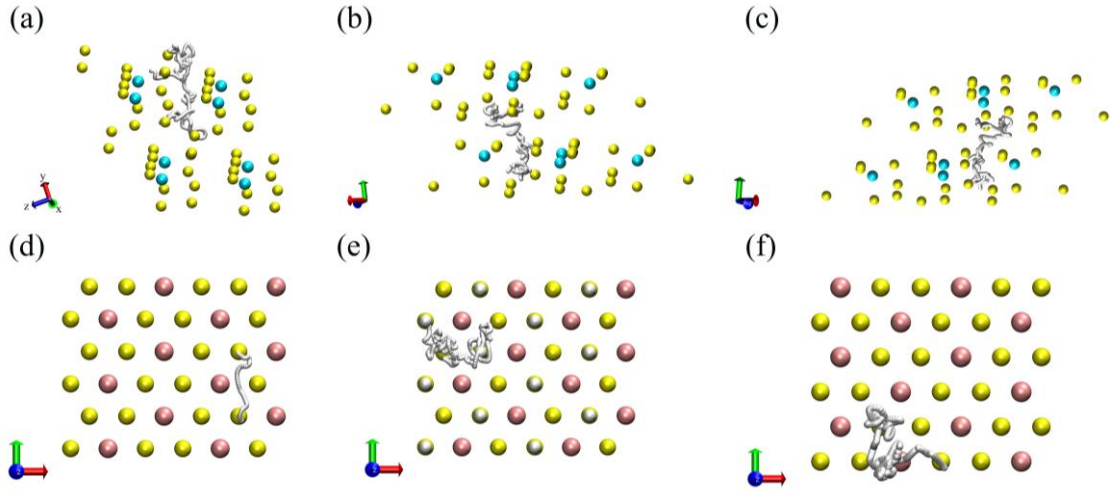

Fig. S6 (a)-(c) The complex three-dimensional diffusion path of Ag_9AlS_6 involves Ag ions freely traversing between sublattices and S ions; (d)-(f) In $AgFeS_2$, the Ag ions exhibit two-dimensional diffusion, and there are three diffusion paths for them.

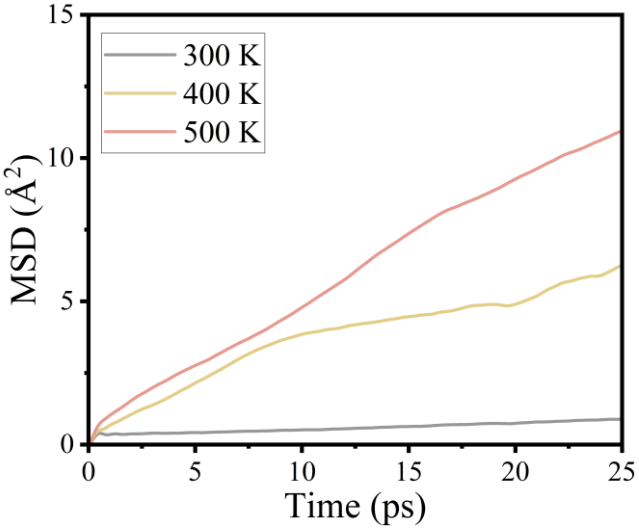

Fig. S7 Under magnetic conditions, the mean square displacements (MSD) of $AgFeS_2$.

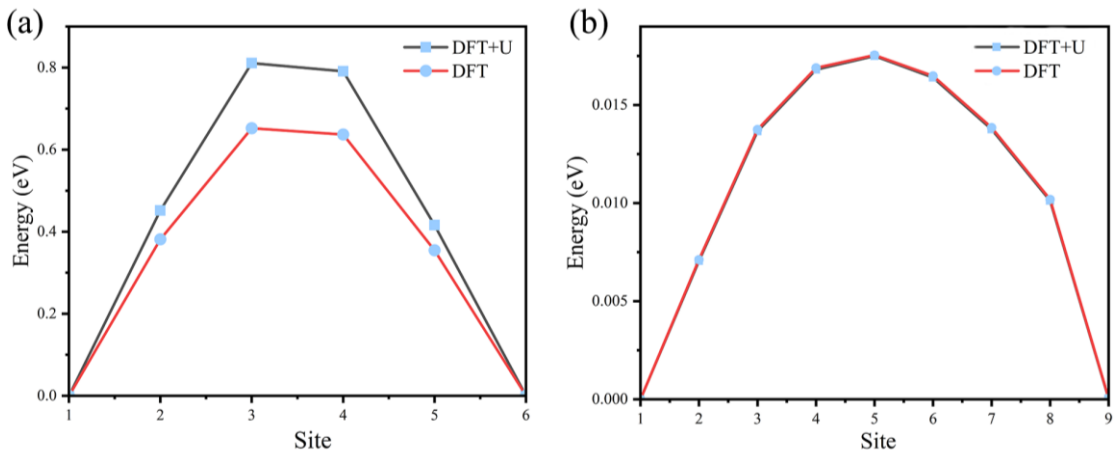

Fig. S8 Calculation of the single-point energy of the Ag ion migration barrier under the DFT + U calculation method (a) $AgFeS_2$ (b) $AgCrS_2$.

Table S2 | The lattice constants of the structures selected through high-throughput screening.

Space group symmetry	Lattice parameter		Atom	Site	Wyckoff atomic coordinate		
					x	y	z
$AgFeS_2$-160	a = 3.409	α = 90.000	Fe1	3a	-0.333	0.333	0.332
(*R*3*m*)	b = 3.409	β = 90.000	Ag1	3a	-0.333	0.333	0.179
(mp-1096969)	c = 19.815	γ = 120.000	S1	3a	-0.333	0.333	0.057
			S2	3a	0	0	0.274
Ag_9AlS_6-1	a = 7.577	α = 63.503	Al1	1a	0.525	0.467	0.511
(*P*1)	b = 7.841	β = 62.660	Ag1	1a	0.455	0.014	0.496
(mp-675325)	c = 7.913	γ = 61.178	Ag2	1a	0.017	0.459	0.038
			Ag3	1a	0.026	0.083	0.400
			Ag4	1a	0.061	0.423	0.476
			Ag5	1a	0.814	0.781	0.240
			Ag6	1a	0.246	0.779	0.156
			Ag7	1a	0.292	0.141	0.848
			Ag8	1a	0.097	0.839	0.780
			Ag9	1a	0.685	0.410	0.960
			S1	1a	0.298	0.242	0.215
			S2	1a	0.608	0.615	0.174
			S3	1a	0.651	0.124	0.604
			S4	1a	0.650	0.607	0.611
			S5	1a	0.163	0.583	0.639
			S6	1a	0.970	0.044	0.994
Ag_7TaS_6-1	a = 7.561	α = 92.049	Ta1	1a	0.988	0.484	0.508
(mp-674352)	b = 7.552	β = 118.493	Ag1	1a	0.888	0.272	0.875
	c = 7.587	γ = 118.295	Ag2	1a	0.449	0.195	0.097
			Ag3	1a	0.077	0.726	0.061
			Ag4	1a	0.613	0.613	0.680
			Ag5	1a	0.056	0.176	0.282
			Ag6	1a	0.097	0.970	0.616
			Ag7	1a	0.417	0.022	0.484
			S1	1a	0.001	0.003	0.958
			S2	1a	0.523	0.283	0.787
			S3	1a	0.750	0.112	0.374
			S4	1a	0.733	0.600	0.394
			S5	1a	0.228	0.597	0.869
			S6	1a	0.243	0.615	0.387
$AgCrS_2$-160	a = 2.998	α = 90.000	Cr1	3a	0	0	0.145
(*R*3*m*)	b = 2.998	β = 90.000	Ag1	3a	0.667	0.333	0.306
(mp-560676)	c = 28.545	γ = 120.000	S1	3a	0.667	0.333	0.197
			S2	3a	0.667	0.333	0.093
Ag_7NbS_6-1	a = 7.591	α = 91.464	Nb1	1a	0.988	0.484	0.512
(*P*1)	b = 7.466	β = 118.930	Ag1	1a	0.885	0.273	0.866
(mp-676348)	c = 7.636	γ = 118.052	Ag2	1a	0.452	0.204	0.091
			Ag3	1a	0.094	0.729	0.069
			Ag4	1a	0.635	0.630	0.693

			Ag5	1a	0.027	0.176	0.268
			Ag6	1a	0.099	0.972	0.609
			Ag7	1a	0.416	0.021	0.485
			S1	1a	0.011	0.008	0.973
			S2	1a	0.522	0.283	0.786
			S3	1a	0.742	0.108	0.378
			S4	1a	0.736	0.604	0.398
			S5	1a	0.230	0.595	0.871
			S6	1a	0.245	0.609	0.393
Ag_6NbS_6-7 (*Pc*) (mp-3926)	a = 7.715 b = 7.434 c = 13.313	α = 90.000 β = 124.766 γ = 90.000	Nb1	2a	1.007	-0.756	0.503
			Ag1	2a	0.106	-0.121	0.410
			Ag3	2a	-0.520	-0.043	0.151
			Ag5	2a	-0.085	-0.399	0.195
			Ag7	2a	0.311	-0.217	0.282
			Ag9	2a	0.698	-0.319	0.733
			Ag11	2a	1.308	-0.513	0.990
			Ag13	2a	0.719	-0.415	0.455
			S1	2a	-0.490	-0.785	0.013
			S3	2a	0.749	-0.733	0.784
			S5	2a	1.148	-0.502	0.632
			S7	2a	1.119	-0.022	0.614
			S9	2a	0.108	-0.755	0.368
			S11	2a	0.645	-0.757	0.399
Ag_5SbS_4-36 ($Cmc2_1$) (mp-4004)	a = 7.763 b = 12.488 c = 9.119	α = 90.000 β = 90.000 γ = 90.000	Ag1	8b	0.803	0.065	0.320
			Ag5	8b	0.313	0.116	0.009
			S1	8b	0.264	0.770	0.283
			Ag9	4a	0.500	0.363	0.178
			Sb1	4a	0.500	0.825	0.118
			S5	4a	0.500	0.018	0.197
			S7	4a	0.500	0.517	0.010

References

[1] R. Jinnouchi, J. Lahnsteiner, F. Karsai, G. Kresse, M. Bokdam, Phase Transitions of Hybrid Perovskites Simulated by Machine-Learning Force Fields Trained on the Fly with Bayesian Inference, Phys. Rev. Lett. 122 (2019) 225701. https://doi.org/10.1103/PhysRevLett.122.225701

[2] R. Jinnouchi, F. Karsai, C. Verdi, R. Asahi, G. Kresse, Descriptors representing two- and three-body atomic distributions and their effects on the accuracy of machine-learned inter-atomic potentials, The Journal of Chemical Physics 152 (2020) 234102. https://doi.org/10.1063/5.0009491

[3] R. Jinnouchi, F. Karsai, G. Kresse, On-the-fly machine learning force field generation: Application to melting points, Phys. Rev. B 100 (2019) 014105. https://doi.org/10.1103/PhysRevB.100.014105

[4] A.V. Shapeev, Moment Tensor Potentials: A Class of Systematically Improvable Interatomic Potentials, Multiscale Model. Simul. 14 (2016) 1153–1173. https://doi.org/10.1137/15M1054183

[5] C. Schran, F.L. Thiemann, P. Rowe, E.A. Müller, O. Marsalek, A. Michaelides, Machine learning potentials for complex aqueous systems made simple, Proc. Natl. Acad. Sci. U.S.A. 118 (2021) e2110077118. https://doi.org/10.1073/pnas.2110077118

[6] M. Rupp, A. Tkatchenko, K.-R. Müller, O.A. Von Lilienfeld, Fast and Accurate Modeling of Molecular

Atomization Energies with Machine Learning, Phys. Rev. Lett. 108 (2012) 058301. https://doi.org/10.1103/PhysRevLett.108.058301

[7] K. Miwa, H. Ohno, Molecular dynamics study on β-phase vanadium monohydride with machine learning potential, PHYSICAL REVIEW B (2016)

[8] Z. Li, J.R. Kermode, A. De Vita, Molecular Dynamics with On-the-Fly Machine Learning of Quantum-Mechanical Forces, Phys. Rev. Lett. 114 (2015) 096405. https://doi.org/10.1103/PhysRevLett.114.096405

[9] C. Chizallet, C. Bouchy, K. Larmier, G. Pirngruber, Molecular Views on Mechanisms of Brønsted Acid-Catalyzed Reactions in Zeolites, Chem. Rev. 123 (2023) 6107–6196. https://doi.org/10.1021/acs.chemrev.2c00896

[10] J. Behler, M. Parrinello, Generalized Neural-Network Representation of High-Dimensional Potential-Energy Surfaces, Phys. Rev. Lett. 98 (2007) 146401. https://doi.org/10.1103/PhysRevLett.98.146401

[11] J. Behler, Neural network potential-energy surfaces in chemistry: a tool for large-scale simulations, Phys. Chem. Chem. Phys. 13 (2011) 17930. https://doi.org/10.1039/c1cp21668f

[12] J. Behler, First Principles Neural Network Potentials for Reactive Simulations of Large Molecular and Condensed Systems, Angew. Chem. Int. Ed. (2017)

[13] A.P. Bartok, M.C. Payne, R. Kondor, G. Csanyi, Gaussian Approximation Potentials: The Accuracy of Quantum Mechanics, without the Electrons, Physical Review Letters (2010)

[14] M.D. Allendorf, Challenges to developing materials for the transport and storage of hydrogen, Nature Chemistry 14 (2022)

[15] M. Zhu, J. Li, M. Lu, Y. Lv, Z. Zhang, Y. Liu, J. Yuan, J. Lin, X. Wang, Alkaline Earth Metal Ions Dynamics in Mixed Ionic-Electronic Conductors of Graphite Intercalation Compounds, Inorg. Chem. (2025) acs.inorgchem.4c05218. https://doi.org/10.1021/acs.inorgchem.4c05218

[16] Y. Lv, J. Li, Z. Zhang, Y. Geng, Y. Liu, J. Yuan, Q. Hu, X. Wang, Superionic conduit of alkaline earth metals confined by two-dimensional boron–carbon layers, Applied Physics Letters 126 (2025) 052201. https://doi.org/10.1063/5.0251023

[17] T.F. Willems, C.H. Rycroft, M. Kazi, J.C. Meza, M. Haranczyk, Algorithms and tools for high-throughput geometry-based analysis of crystalline porous materials, Microporous and Mesoporous Materials 149 (2012) 134–141. https://doi.org/10.1016/j.micromeso.2011.08.020

[18] A. Jain, S.P. Ong, G. Hautier, W. Chen, W.D. Richards, S. Dacek, S. Cholia, D. Gunter, D. Skinner, G. Ceder, K.A. Persson, Commentary: The Materials Project: A materials genome approach to accelerating materials innovation, APL Materials 1 (2013) 011002. https://doi.org/10.1063/1.4812323

[19] S.P. Ong, W.D. Richards, A. Jain, G. Hautier, M. Kocher, S. Cholia, D. Gunter, V.L. Chevrier, K.A. Persson, G. Ceder, Python Materials Genomics (pymatgen): A robust, open-source python library for materials analysis, Computational Materials Science 68 (2013) 314–319. https://doi.org/10.1016/j.commatsci.2012.10.028

[20] L.H. Ahrens, The use of ionization potentials Part 1. Ionic radii of the elements, Geochimica et Cosmochimica Acta 2 (1952) 155–169. https://doi.org/10.1016/0016-7037(52)90004-5

[21] L. Pauling, G.W. Wheland, The Nature of the Chemical Bond. V, The Journal of Chemical Physics 2 (1934) 482–482. https://doi.org/10.1063/1.1749514

[22] J. Luo, Y. Zhang, X. Cheng, F. Li, H. Tan, M. Zhou, Z. Wang, X. Hao, Y. Yin, B. Jiang, H. Yao, Halide Superionic Conductors with Non-Close-Packed Anion Frameworks, Angew Chem Int Ed 63 (2024) e202400424. https://doi.org/10.1002/anie.202400424

[23] X. He, Y. Zhu, Y. Mo, Origin of fast ion diffusion in super-ionic conductors, Nat Commun 8 (2017) 15893. https://doi.org/10.1038/ncomms15893

[24] S. Wenzel, S. Randau, T. Leichtweiß, D.A. Weber, J. Sann, W.G. Zeier, J. Janek, Direct Observation of the Interfacial Instability of the Fast Ionic Conductor $Li_{10}GeP_2S_{12}$ at the Lithium Metal Anode, Chem. Mater. 28

(2016) 2400–2407. https://doi.org/10.1021/acs.chemmater.6b00610

[25] R. Jalem, Y. Yamamoto, H. Shiiba, M. Nakayama, H. Munakata, T. Kasuga, K. Kanamura, Concerted Migration Mechanism in the Li Ion Dynamics of Garnet-Type $Li_7 La_3 Zr_2 O_{12}$, Chem. Mater. 25 (2013) 425–430. https://doi.org/10.1021/cm303542x

[26] S. Hull, P. Berastegui, A. Grippa, Ag^+ diffusion within the rock-salt structured superionic conductor $Ag_4 Sn_3 S_8$, J. Phys.: Condens. Matter 17 (2005) 1067–1084. https://doi.org/10.1088/0953-8984/17/7/002

[27] T.M. Hayes, J.B. Boyce, J.L. Beeby, A structural model for superionic conduction, J. Phys. C: Solid State Phys. 11 (1978) 2931–2937. https://doi.org/10.1088/0022-3719/11/14/016

[28] M. Murayama, R. Kanno, Y. Kawamoto, T. Kamiyama, Structure of the thio-LISICON, Li4GeS4, Solid State Ionics 154–155 (2002) 789–794. https://doi.org/10.1016/S0167-2738(02)00492-7

[29] M. Parrinello, A. Rahman, P. Vashishta, Structural Transitions in Superionic Conductors, Phys. Rev. Lett. 50 (1983) 1073–1076. https://doi.org/10.1103/PhysRevLett.50.1073

[30] J.B. Boyce, B.A. Huberman, Superionic conductors: Transitions, structures, dynamics, Physics Reports 51 (1979) 189–265. https://doi.org/10.1016/0370-1573(79)90067-X

[31] J.H. MacNeil, D.M. Massi, J.-H. Zhang, K.A. Rosmus, C.D. Brunetta, T.A. Gentile, J.A. Aitken, Synthesis, structure, physicochemical characterization and electronic structure of thio-lithium super ionic conductors, Li4GeS4 and Li4SnS4, Journal of Alloys and Compounds 586 (2014) 736–744. https://doi.org/10.1016/j.jallcom.2013.10.011

[32] I.-H. Chu, C.S. Kompella, H. Nguyen, Z. Zhu, S. Hy, Z. Deng, Y.S. Meng, S.P. Ong, Room-Temperature All-solid-state Rechargeable Sodium-ion Batteries with a Cl-doped Na3PS4 Superionic Conductor, Sci Rep 6 (2016) 33733. https://doi.org/10.1038/srep33733

[33] H. Wang, Y. Chen, Z.D. Hood, G. Sahu, A.S. Pandian, J.K. Keum, K. An, C. Liang, An Air-Stable $Na_3 SbS_4$ Superionic Conductor Prepared by a Rapid and Economic Synthetic Procedure, Angewandte Chemie 128 (2016) 8693–8697. https://doi.org/10.1002/ange.201601546

[34] R. Li, K. Xu, S. Wen, X. Tang, Z. Lin, X. Guo, M. Avdeev, Z. Zhang, Y.-S. Hu, A sodium superionic chloride electrolyte driven by paddle wheel mechanism for solid state batteries, Nat Commun 16 (2025) 6633. https://doi.org/10.1038/s41467-025-61738-6

[35] R. Xiao, H. Li, L. Chen, High-throughput computational discovery of K2CdO2 as an ion conductor for solid-state potassium-ion batteries, J. Mater. Chem. A 8 (2020) 5157–5162. https://doi.org/10.1039/C9TA13105A

[36] J. Shao, J. Zheng, L. Qin, S. Zhang, Y. Ren, Y. Wu, $K_3 SbS_4$ as a Potassium Superionic Conductor with Low Activation Energy for K–S Batteries, Angew Chem Int Ed 61 (2022) e202200606. https://doi.org/10.1002/anie.202200606

[37] H. Suyama, S. Sato, T. Matsunaga, T. Inoue, A. Ikezawa, H. Arai, Anticrystallization and Superionic Conduction of Highly Concentrated Potassium Pyrophosphate Aqueous Electrolytes, ACS Appl. Energy Mater. 6 (2023) 11897–11905. https://doi.org/10.1021/acsaem.3c01861